Vertical cracks characterization using lock-in thermography: I. Infinite cracks.

N.W. Pech-May[1,2], A. Oleaga[1], A. Mendioroz[1], A.J. Omella[3], R. Celorrio[3] and A. Salazar[1]

[1]Departamento de Física Aplicada I, Escuela Técnica Superior de Ingeniería, Universidad del País Vasco UPV/EHU, Alameda Urquijo s/n, 48013 Bilbao, Spain

[2]Department of Applied Physics, CINVESTAV Unidad Mérida, carretera Antigua a Progreso km6, A.P. 73 Cordemex, Mérida Yucatán 97310, México

[3]Departamento de Matemática Aplicada, EINA/IUMA, Universidad de Zaragoza, Campus Río Ebro, Edificio Torres Quevedo, 50018 Zaragoza, Spain

E-mail: **agustin.salazar@ehu.es**

Abstract

Early detection of cracks is a challenging task to prevent failures in working structures. In the last decades the "flying spot" method, based on heating the sample with a moving laser spot and detecting the surface temperature with an infrared detector, has been developed to detect cracks in a fast manner. The aim of this work is to measure the width of an infinite vertical crack using lock-in thermography. An analytical solution for the surface temperature of a sample containing such a crack when the surface is illuminated by a modulated and focused laser spot close to the crack is obtained. Measurements on samples containing calibrated cracks have been performed using an infrared camera. A least square fit of the amplitude and phase of the surface temperature is used to retrieve the thickness of the crack. A very good agreement between the nominal and retrieved thickness of fissure is found, even for widths down to 1 μm, confirming the validity of the model.

Keywords: infrared thermography, crack detection, thermal waves, nondestructive evaluation.

PACS numbers: 66.70.+f 81.70.Fy 44.10.+I 66.30.Xj

1. Introduction

Early detection of both hidden and surface breaking cracks is a challenging task to prevent failures in working structures. Conventional nondestructive testing methods like dye penetrant, magnetic particles, eddy currents, and x-ray have been widely used to detect fissures. Since the pioneering work by Kubiak [1] infrared thermography has been proposed as a noncontact, nonintrusive and health safe method to detect near-surface defects. Vibrothermography, where an ultrasonic wave is launched into the material and the heat dissipated at the defect propagates to the surface indicating the presence of the defect on a cold background, has received an increasing attention in the last decade because of its ability to detect and characterize cracks in a wide variety of materials [2-7]. However, in this technique the ultrasonic transducer must be coupled to the sample surface, thus reducing the versatility of this technique. Moreover, open cracks with virtually no rubbing surfaces might be difficult to characterize [8]. Optically stimulated thermography is fully noncontact instead, but the presence of the defect produces just a perturbation of the existing surface temperature field, generated by the external excitation. In addition, the spatial configuration of the illumination strongly affects the detectability of cracks. In the case of vertical cracks, if the sample is excited by a homogeneous illumination producing a heat flux perpendicular to the sample surface, the crack will barely disperse the flux thus producing a negligible signature on the surface temperature distribution. This kind of cracks can be detected only when an asymmetry in the heat flux is produced. In this way, the so-called flying spot method was introduced in the early nineties [9]. It is based on heating the sample with a moving laser spot or line and detecting the time evolution of the surface temperature with an infrared camera [10-16]. This technique has been implemented for different excitation regimes, mostly continuous wave [9-12] and pulsed illuminations [13-16] and, less often, modulated [14] excitations. Using this method, cracks with openings as small as a few micrometers can be detected [13]. In the last years several approaches to characterize the geometrical parameters of the crack (depth, length, width, orientation…) have been published [17-18]. They take advantage of the asymmetry of the temperature field at both sides of the crack arising from the thermal resistance produced by the crack, which partially blocks heat flux when the laser spot is focused close to the crack.

In Part I of this work, we deal with the characterization of infinite vertical cracks using lock-in thermography, which is able to provide surface temperature amplitude and phase images with a very low noise level. First, we have found an analytical expression for the surface temperature of a sample containing such a crack when the surface is illuminated by a modulated and focused laser spot close to the crack. Two geometries of the laser spot are considered: a circular Gaussian spot and a line Gaussian one. The presence of the defect produces an abrupt jump in the amplitude and phase of the temperature profile at the crack position. The influence of the experimental parameters (laser beam radius, distance spot-crack, modulation frequency and width of the crack) on the jump height is analyzed. The goal is to measure the thermal contact resistance R_{th} of the crack, which quantifies the width of the crack.

In order to prepare calibrated infinite vertical cracks, very thin metallic tapes down to 1 μm thick are inserted between two identical blocks under pressure. A modulated laser beam is focused close to the crack. An infrared video camera equipped with a lock-in module provides the amplitude and phase of the surface temperature around the crack. A microscope lens with a spatial resolution of 30 μm is used to collect the infrared emission from the sample. A least square fit of the temperature profile crossing the center of the laser spot and perpendicular to the crack is used to retrieve R_{th}. A very good agreement between the thickness of the metallic tapes and the obtained R_{th} is found, confirming the validity of the

model. Moreover, by putting the two blocks directly in contact an extremely narrow crack is obtained that remains undetectable for our thermography setup. We can establish that the upper limit for the thermal resistance of this crack is $R_{th} \leq 10^{-6}$ m^{2}K/W.

In Part II of this work, we deal with vertical cracks of finite size and arbitrary shape. In this case there is no analytical solution for the temperature field. We have developed a discontinuous finite element method which allows us to calculate the surface temperature distribution in the presence of cracks of any size, shape and thickness. Discontinuous finite elements is a natural tool to tackle physical problems with discontinuous solutions where classical finite element methods fail [19].

2. Theory

Let us consider a semi-infinite and opaque material with an infinite vertical crack placed at plane $y = 0$. The sample surface is illuminated by a laser beam modulated at a frequency f ($\omega = 2\pi f$). The center of the laser spot is located at a distance d from the crack. The geometry of the problem is shown in Fig. 1. We assume adiabatic boundary conditions at the sample surface, i.e. heat losses to the surrounding air are neglected. Two kinds of laser profiles are used: (a) a circular Gaussian profile of radius a (at $1/e^2$ of the intensity) and (b) a line Gaussian profile of width a. The aim of this section is to calculate how the crack modifies the surface temperature distribution.

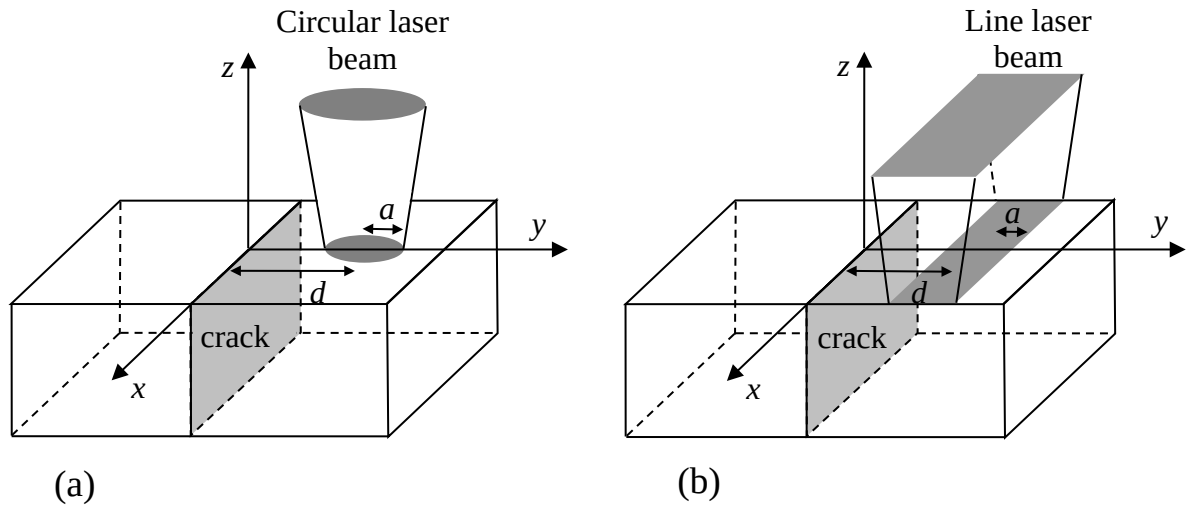

Figure 1. Scheme of the infinite vertical crack (in gray) inside a semi-infinite sample. (a) Circular illumination and (b) line illumination.

2.1. Circular Gaussian illumination

Let us start considering an infinite material containing an infinite crack at plane $y = 0$, together with a modulated point-like heat source located at $(0,d,0)$, whose maximum power is P_o, see Fig. 1a. The expressions for the spherical thermal wave T generated at the heat source, and the thermal waves scattered at the crack travelling through $y > 0$ and $y < 0$, τ_+ and τ_- respectively, are given by [20,21]

$$T(x,y,z) = \frac{P_o}{4\pi K}\frac{e^{-qR}}{R} = \frac{P_o}{4\pi K}\int_0^\infty \delta J_o(\delta r)\frac{e^{-\beta|y-d|}}{\beta}d\delta \quad (1)$$

$$\tau_+(x,y,z) = P_o\int_0^\infty \delta J_o(\delta r)Ae^{-\beta y}d\delta \quad (2)$$

$$\tau_-(x,y,z) = P_o\int_0^\infty \delta J_o(\delta r)Be^{\beta y}d\delta\,, \quad (3)$$

where $q = \sqrt{i\omega/D}$ is the thermal wave vector, K and D the thermal conductivity and diffusivity of the material respectively, $\beta = \sqrt{\delta^2 + q^2}$, $R = \sqrt{x^2 + (y-d)^2 + z^2}$ and $r = \sqrt{x^2 + z^2}$. Note that the last expression in Eq. (1) represents a spherical thermal wave in the Hankel space. The temperature of the material at y > 0 is given by $T_+ = T + \tau_+$, and the temperature of the material at y < 0 by $T_- = T + \tau_-$. Finally, the values of A and B are determined from the boundary conditions at the crack: heat flux continuity and temperature discontinuity due to the lack of thermal contact:

$$-K\left.\frac{dT_+}{dy}\right|_{y=0} = -K\left.\frac{dT_-}{dy}\right|_{y=0} \quad (4)$$

$$(T_+ - T_-)_{y=0} = R_{th}K\left.\frac{dT_+}{dy}\right|_{y=0}\,, \quad (5)$$

where R_{th} is the thermal contact resistance of the crack, which is related to the air gap L through the equation $R_{th} = L/K_{air}$ [22]. By solving Eqs. (4) and (5) we obtain

$$A = -B = \frac{R_{th}}{4\pi}\frac{e^{-\beta|d|}}{2 + R_{th}K\beta}\frac{d}{|d|}. \quad (6)$$

Accordingly, the temperature inside the material at both sides of the crack is given by

$$T_\pm(x,y,z) = \frac{P_o}{4\pi K}\frac{e^{-qR}}{R} \pm P_o\int_0^\infty \delta J_o(\delta r)Ae^{\mp\beta y}d\delta\,. \quad (7)$$

As a further step we consider now a semi-infinite sample whose free surface is located at plane $z = 0$. By applying the image method, the temperature in the material is twice the value given by Eq. (7) for the infinite material

$$T_\pm(x,y,z) = \frac{P_o}{2\pi K}\frac{e^{-qR}}{R} \pm 2P_o\int_0^\infty \delta J_o(\delta r)Ae^{\mp\beta y}d\delta \quad (8)$$

Finally if we consider not an ideal point-like heat source but a real circular Gaussian spot of total maximum power P_o and radius a (at $1/e^2$ of the intensity), the temperature inside the material is obtained by adding the contribution of each point of the Gaussian spot weighted by its intensity

$$T_\pm(x,y,z) = \frac{P_o}{\pi^2 a^2 K}\int_{-\infty}^{\infty}\int_{-\infty}^{\infty} dx_o dy_o e^{-\frac{2\left[x_o^2 + (y_o-d)^2\right]}{a^2}}\left[\frac{e^{-qR_o}}{R_o} \pm KR_{th}\frac{y_o}{|y_o|}\int_0^\infty \delta J_o(\delta r_o)\frac{e^{-\beta(|y_o|+|y|)}}{2 + KR_{th}\beta}d\delta\right] \quad (9)$$

where $R_o = \sqrt{(x-x_o)^2 + (y-y_o)^2 + z^2}$ and $r_o = \sqrt{(x-x_o)^2 + z^2}$. Equation (9) gives the temperature at any point of the semi-infinite material but its numerical evaluation is rather time consuming since a triple integral is concerned. By considering the surface temperature profile along the y axis, i.e. perpendicular to the crack and crossing the center of the laser spot, the order of the integrals drops, drastically reducing the computing time.

$$T_\pm(0,y,0) = \frac{P_o}{\pi^2 a^2 K}\int_{-\infty}^{\infty}\int_{-\infty}^{\infty} dx_o dy_o e^{-\frac{2\left[x_o^2 + (y_o-d)^2\right]}{a^2}}\frac{e^{-qR_1}}{R_1} \pm$$

$$\pm\frac{P_o}{4\pi K}KR_{th}\int_0^\infty e^{-\frac{(\delta a)^2}{16}}I_o\left[\frac{(\delta a)^2}{16}\right]\frac{e^{(\frac{a^2\beta^2}{8}-\beta d-\beta|y|)}}{2+KR_{th}\beta}\left[1-erf\left(\frac{a^2\beta-4d}{2\sqrt{2}a}\right)-e^{2\beta d}erfc\left(\frac{a^2\beta+4d}{2\sqrt{2}a}\right)\right]\delta d\delta \tag{10}$$

Here $R_1=\sqrt{x_o^2+(y-y_o)^2}$, I_o is the modified Bessel function of order zero, *erf* is the error function, and *erfc* is the complementary error function [23].

2.2. Line Gaussian illumination

The geometry we are dealing with is shown in Fig. 1b. As in the previous subsection let us start considering an infinite material containing an infinite crack at plane $y = 0$. It is heated by an infinitely thin modulated line heat source located at $y = d$, whose maximum power per unit length is P'_o The expressions for the cylindrical thermal wave T generated at the heat source, and the thermal waves scattered at the crack travelling through $y > 0$ and $y < 0$, τ_+ and τ_- respectively, are

$$T(y,z)=\frac{P'_o}{4\pi K}K_o(qR_2)=\frac{P'_o}{4\pi K}\int_0^\infty cos(\delta z)\frac{e^{-\beta|y-d|}}{\beta}d\delta, \tag{11}$$

$$\tau_+(y,z)=P'_o\int_0^\infty \cos(\delta z)Ae^{-\beta y}d\delta, \tag{12}$$

$$\tau_-(y,z)=P'_o\int_0^\infty \cos(\delta z)Be^{\beta y}d\delta, \tag{13}$$

where $R_2=\sqrt{(y-d)^2+z^2}$ and K_o is the modified Bessel function of the second kind order zero. The last expression in Eq. (11) represents a cylindrical thermal wave in the Fourier space. The temperature of the material at $y > 0$ is given by $T_+ = T+\tau_+$, and the temperature of the material at y < 0 by $T_- = T+\tau_-$. Using the boundary conditions at the crack given by Eqs. (4) and (5) we obtain the same values of A and B given Eq. (6).

Accordingly, the temperature inside the material at both sides of the crack is given by

$$T_\pm(y,z)=\frac{P'_o}{4\pi K}K_o(qR_2)\pm P'_o\int_0^\infty \cos(\delta z)Ae^{\mp\beta y}d\delta. \tag{14}$$

For a semi-infinite material whose free surface is located at plane $z = 0$ the temperature is twice the value given by Eq. (14) for the infinite material

$$T_\pm(y,z)=\frac{P'_o}{2\pi K}K_o(qR_2)\pm 2P'_o\int_0^\infty \cos(\delta z)Ae^{\mp\beta y}d\delta. \tag{15}$$

Finally if we consider not an ideal infinitely thin line heat source but a real line Gaussian spot of total power per unit length P'_o and radius a (at $1/e^2$ of the intensity), the temperature inside the material is obtained by adding the contribution of each line of the Gaussian spot weighted by its intensity

$$T_\pm(y,z)=\sqrt{\frac{2}{\pi}}\frac{P'_o}{Ka}\int_\infty^\infty dy_o e^{-\frac{2(y_o-d)^2}{a^2}}\left[\frac{K_o(qR_3)}{2\pi}\pm\int_0^\infty\cos(\delta z)\frac{KR_{th}}{2\pi}\frac{e^{-\beta(|y_o|+|y|)}}{2+KR_{th}\beta}\frac{y_o}{|y_o|}d\delta\right], \tag{16}$$

where $R_3=\sqrt{(y-y_o)^2+z^2}$.

If we confine the temperature calculations to the surface of the sample (z = 0) the order of the integrals is reduced

$$T_\pm(y,0)=\frac{P'_o}{\sqrt{2\pi^3}Ka}\int_\infty^\infty dy_o e^{-\frac{2(y_o-d)^2}{a^2}}K_o(qR_4)\pm$$

$$\pm\frac{P'_o}{4\pi K} KR_{th} \int_0^\infty \frac{e^{\left(\frac{a^2\beta^2}{8} - \beta d - \beta|y|\right)}}{2 + KR_{th}\beta} \left[1 - erf\left(\frac{a^2\beta - 4d}{2\sqrt{2}a}\right) - e^{2\beta d} erfc\left(\frac{a^2\beta + 4d}{2\sqrt{2}a}\right)\right] d\delta, \qquad (17)$$

where $R_4 = \sqrt{(y - y_o)^2}$.

3. Numerical simulations

In this section, we analyze how the presence of a vertical crack modifies the surface temperature of a semi-infinite sample. The influence of parameters *d*, *a* and *f* in the visibility of the crack is studied. All the simulations are performed for AISI-304 stainless steel (D = 4.0 mm^2/s and K = 15 Wm^{-1}K^{-1}). Figure 2 shows the calculation of the natural logarithm of the temperature amplitude Ln|*T*| and phase Ψ along the *y* axis for a semi-infinite AISI-304 sample containing an infinite vertical crack (y = 0) and illuminated by a circular Gaussian spot. Calculations are performed using Eq. (10) with d = 1 mm, a = 0.75 mm and f = 1 Hz. Four thermal resistances ranging from 10^{-5} m^{2}K/W to 10^{-2} m^{2}K/W are analyzed. As can be observed, there is an abrupt discontinuity at the crack position in both Ln|*T*| and Ψ. Note that the same scale level is used in Ln|*T*| and Ψ in order to clearly show that the jump at the crack is much higher for the former. Regarding Ln|*T*|, the height of the leap increases with R_{th}. However, the behavior of Ψ is more complicated since for high R_{th} values the phase jump is reversed.

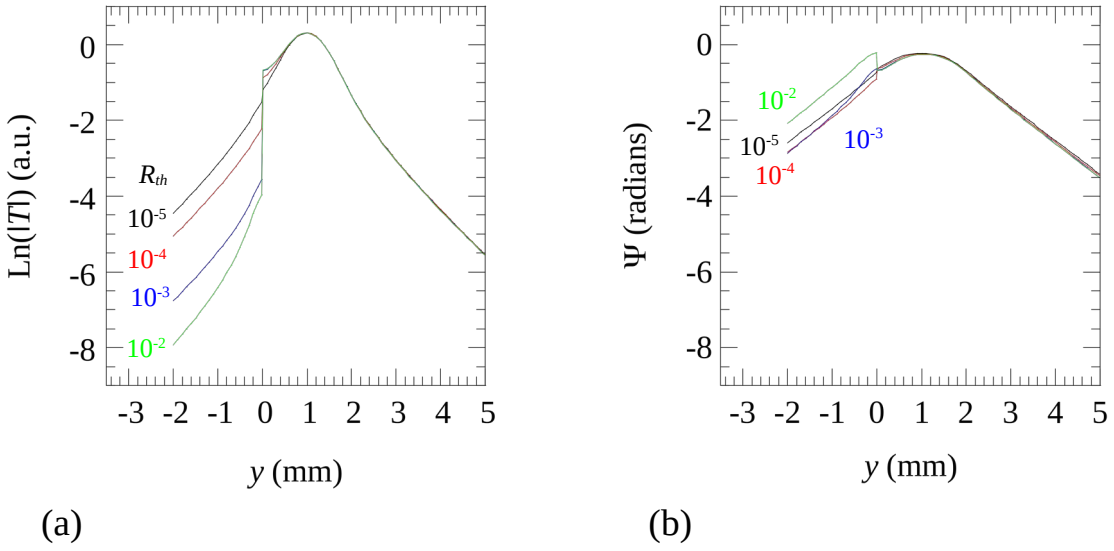

Figure 2. Simulation of (a) the natural logarithm of the temperature amplitude and (b) phase along the *y* axis for a semi-infinite AISI-304 sample (D = 4 mm^2/s and K = 15 Wm^{-1}K^{-1}) containing an infinite vertical crack. The sample is illuminated at d = 1 mm with a circular Gaussian laser with a = 0.75 mm modulated at f = 1 Hz. The effect of the value of the thermal resistance R_{th} (m^{2}K/W) is shown.

Figure 3 shows the same type of simulations as in Fig. 2, but for a line Gaussian laser. Calculations are performed using Eq. (17) with the same parameters as in the previous figure. As can be seen, the general trend is similar for both kinds of illumination. The only remarkable difference between both illuminations is that Ln|*T*| is steeper for circular illumination than for line illumination. This result is related to the fact that for the former a spherical thermal wave is generated while for the later the thermal wave is cylindrical.

Anyway, as the crack jumps are almost the same for both kind of spots, in the remaining of the section only simulations with circular Gaussian illumination are shown.

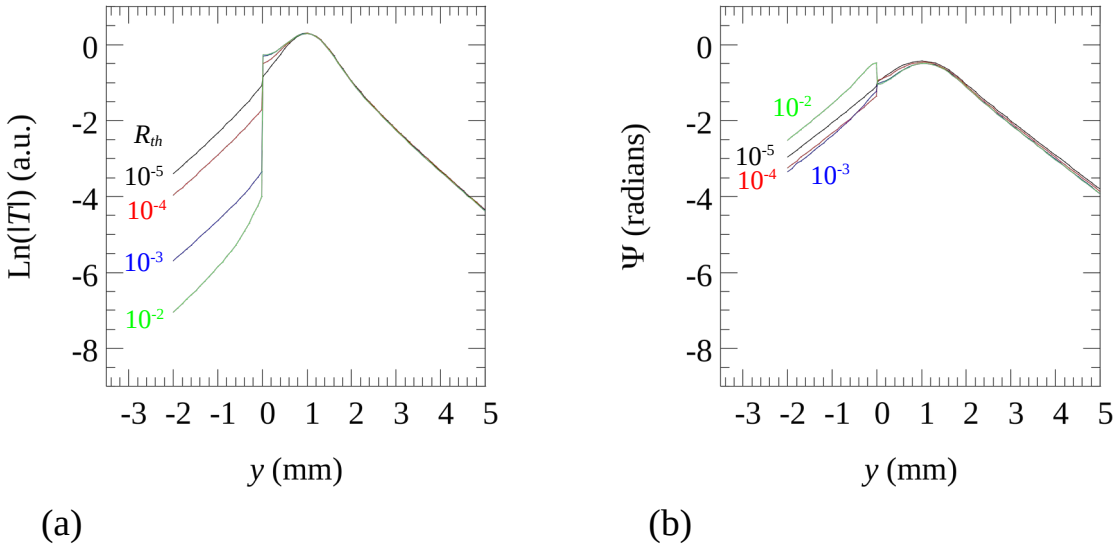

Figure 3. The same as in Fig. 2, but for a line Gaussian laser.

In order to quantify the strength of the temperature jump at the crack position we introduce two parameters: (a) the temperature amplitude contrast at the crack $\Delta_{|T|}$, which is defined as

$$\Delta_{|T|} = \frac{|T_+(0,0,0)| - |T_-(0,0,0)|}{|T_+(0,d,0)|}, \tag{18}$$

and (b) the phase contrast Δ_Ψ, defined as

$$\Delta_\Psi = \Psi_+(0,0,0) - \Psi_-(0,0,0). \tag{19}$$

Eqs. (10) and (17) show that both $\Delta_{|T|}$ and Δ_Ψ depend on the factor KR_{th}. This means that narrow cracks are better detected in high thermal conducting materials (metals, alloys, ceramics…) than in thermal insulators (polymers, composites…). Moreover, $\Delta_{|T|}$ and Δ_Ψ do not depend on the laser power P_o.

First, we analyze the dependence of $\Delta_{|T|}$ and Δ_Ψ on the thermal resistance of the crack. The results are shown in Fig. 4 for d = μ and a = μ/2, where $\mu = \sqrt{D/\pi f}$ is the thermal diffusion length. Three modulation frequencies are tested: 0.01, 1 and 100 Hz. Continuous lines correspond to $\Delta_{|T|}$ and dashed lines to Δ_Ψ. As can be seen, both $\Delta_{|T|}$ and Δ_Ψ exhibit a sigmoid shape. For low R_{th} (very narrow cracks) there is no temperature contrast and the crack remains undetected. For large R_{th} (thick cracks) the temperature contrast saturates, indicating that these cracks are easy to detect, but R_{th} is difficult to quantify. The highest sensitivity to the thermal resistance appears for intermediate R_{th} values. Note that as the modulation frequency is increased by two orders of magnitude, the sensitivity to R_{th} is displaced to lower values by one order of magnitude. This result means that the high frequencies are better suited to detect and characterize thin cracks.

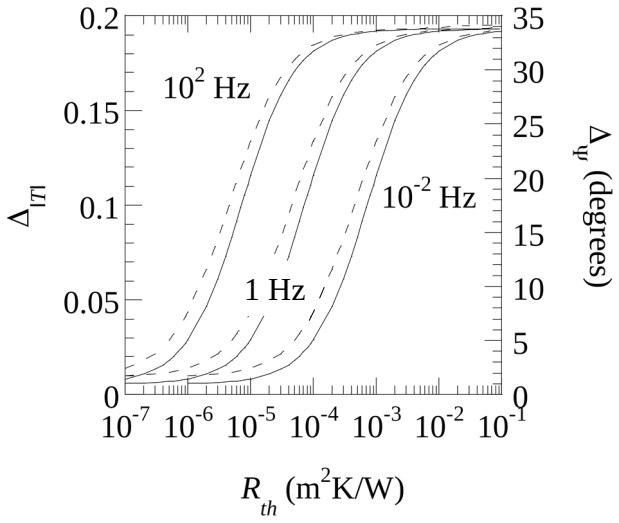

Figure 4. Numerical simulation of the dependence of Δ on the thermal contact resistance R_{th}. Calculations are performed for an AISI-304 material (D = 4 mm^2/s and K = 15 $Wm^{-1}K^{-1}$) with d = μ and a = μ/2. Three modulation frequencies are tested. Continuous lines correspond to $\Delta_{|T|}$ and dashed lines to Δ_Ψ .

Anyway, the results shown in Fig. 4 have no general validity. In Fig. 5 we shown the same kind of calculations as in Fig. 4 for f = 1 Hz and three combinations of d and a: (1) d = μ and a = μ/2, (2) d = μ and a = μ, and (3) d = μ/2 and a = μ/4. As can be seen, the amplitude contrast $\Delta_{|T|}$ is always a sigmoid function, but as a approaches d the shape of the phase contrast Δ_Ψ is no longer a sigmoid. In fact, the phase contrast can be even negative, as it has been shown in Fig. 2b. It is worth noting that for a fixed frequency the region of the highest sensitivity of $\Delta_{|T|}$ to R_{th} (the region with the steepest slope) is independent of the couple (d, a). In fact, it only depends on f.

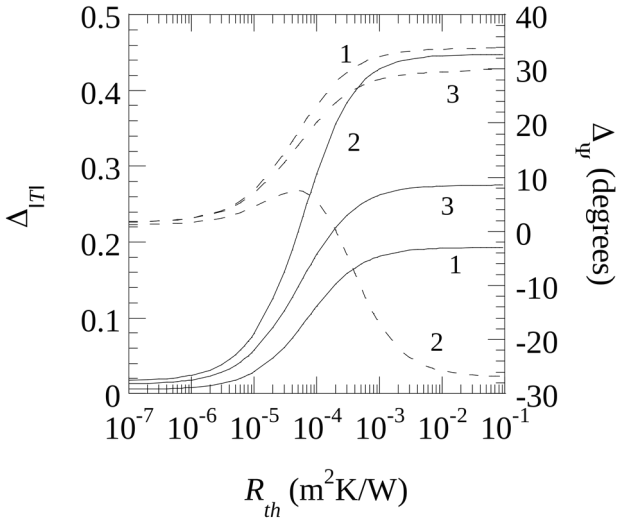

Figure 5. The same as in Fig. 4 with a fixed frequency f = 1 Hz. Continuous lines correspond to $\Delta_{|T|}$ and dashed lines to Δ_{Ψ}. Three combinations of laser distance and radius are analyzed: (1) d = μ and a = μ/2, (2) d = μ and a = μ, and (3) d = μ/2 and a = μ/4.

The dependence of $\Delta_{|T|}$ and Δ_{Ψ} on the laser spot radius is analyzed in Fig. 6. Calculations are performed with d = μ. Three thermal resistances are studied: 10^{-5}, 10^{-4} and 10^{-3} m^2K/W. As can be observed, the highest amplitude contrast corresponds to $a \approx 1.25\mu$, i.e. when the laser spot slightly overlaps the crack. This result is independent of R_{th}. On the other hand, the highest phase contrast appears for a tightly focused laser beam. Note the negative phase contrast for some combinations of R_{th} and a. A negative contrast means that the phase increases at the other side of the crack with respect to the heating spot. This result has already been shown in Fig. 2b for $R_{th} = 10^{-2}$ m^2K/W.

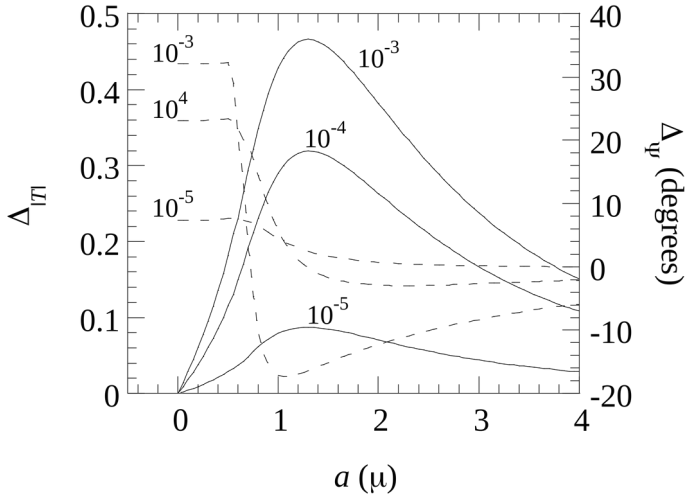

Figure 6. Numerical simulation of the dependence of Δ on the laser radius a. Calculations are performed for an AISI-304 sample with d = μ. Three R_{th} values are analyzed: 10^{-5}, 10^{-4} and 10^{-3} m^2K/W. The continuous line corresponds to $\Delta_{|T|}$ and the dashed line to Δ_{Ψ}.

Finally, in Fig. 7 the dependence of $\Delta_{|T|}$ and Δ_{Ψ} on the distance of the laser spot to the crack is analyzed. Calculations are performed for a fixed laser beam radius a = 0.75μ. The same three thermal resistances as in the previous figure are studied. As expected from Fig. 6, the highest amplitude contrast is produced when the laser spot overlaps the crack $d \approx 0.5\mu \approx 0.7a$. Note that this result is independent of R_{th}. It is worth mentioning that as the laser spot moves away from the crack the contrast in amplitude decreases, but surprisingly the phase contrast increases till it reaches an asymptotic value.

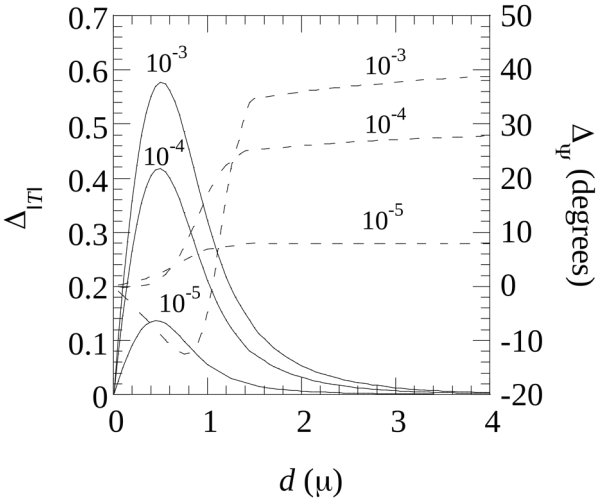

Figure 7. Numerical simulation of the dependence of Δ on the distance of the laser spot to the crack. Calculations have been performed for an AISI-304 sample (D = 4 mm^2/s and K = 15 Wm^{-1}K^{-1}) with a = 0.75μ and f = 1 Hz. Three R_{th} values are analyzed: 10^{-5}, 10^{-4} and 10^{-3} m^{2}K/W. The continuous line corresponds to $\Delta_{|T|}$ and the dashed line to Δ_{ψ}.

According to the simulations shown in this section, we arrive at the following conclusions:

(a) For a given thermal resistance the largest amplitude and phase contrast are not obtained with the same set of experimental parameters (d, a). The highest amplitude contrast appears when the spot slightly overlaps the crack $a \approx 1.25d$. On the other hand, tightly focused spots ($a < d$) produce the highest phase contrast. We propose $d \approx \mu \approx 1.25a$ as a rule of thumb to obtain good enough amplitude and phase contrast simultaneously.

(b) In order to detect very narrow cracks the appropriate experimental conditions are a high frequency with $d \approx a \approx \mu$. These conditions mean a tightly focused laser spot. For instance, using $a = d = 0.1$ mm on metallic samples together with a frequency $f \approx$ 100-1000 Hz allows to detect thermal resistances as low as 10^{-6} - 10^{-7} m^{2}K/W. It is worth noting that under these experimental conditions thicker cracks are also clearly detected.

(c) In order to retrieve R_{th}, frequencies producing the highest temperature amplitude/phase contrast must be avoided, since they are insensitive to R_{th}. Lower frequencies showing an amplitude contrast half of the maximum one are the most sensitive to R_{th} variations.

4. Experimental results

The scheme of the experimental setup is shown in Fig. 8. A continuous wave laser (512 nm), whose intensity is modulated by an acousto-optic modulator, is directed to the sample surface by means of a mirror and a silicon window, which is transparent to IR wavelengths. By means of a 10 cm focal length lens the laser beam is focused onto the sample surface. The laser power is changed at each frequency (50 mW - 200 mW) in order to obtain a similar temperature rise at the center of the laser spot of about 5 K. An IR video camera (FLIR, model SC7500) with an InSb detector operating in the 3 - 5 μm spectral range, records the sample surface temperature. A microscope lens has been used to improve the spatial resolution; each pixel measures the average temperature over a square of 30 μm in side. In order to increase the signal to noise ratio a large number of images have been recorded, since

in lock-in measurements the average noise level in temperature amplitude is given by the following relation [24]

$$\left\langle Noise_{|T|} \right\rangle = \frac{2}{\sqrt{N_{images}}} NETD, \qquad (20)$$

where *NETD* is the Noise Equivalent Temperature Difference of the detector (20 mK in our camera) and N_{images} is the total number of images collected for the lock-in analysis. According to Eq. (20), by processing 2×10^4 images the noise level of the data was kept below 0.3 mK. As our camera works at a maximum rate of 350 images/s, collecting 2×10^4 images requires measurements of about one minute.

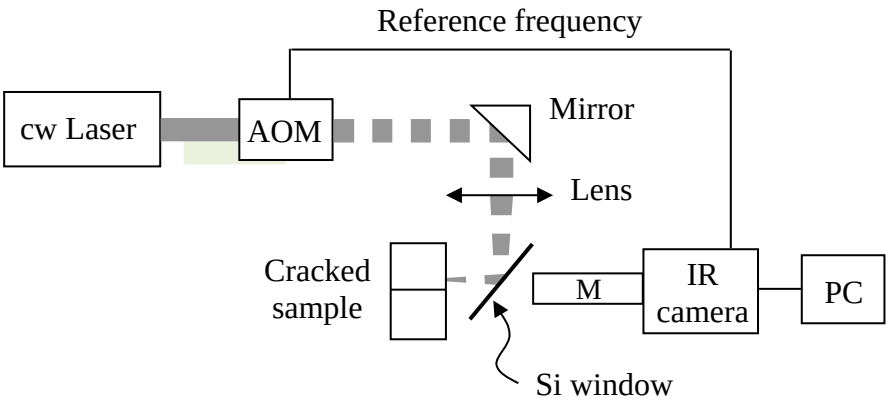

Figure 8. Diagram of the experimental setup. AOM is the acousto-optic modulator and M is the microscope objective.

In order to obtain calibrated vertical cracks we have used two glassy carbon plates (D = 6.0 mm^2/s and K = 6.3 Wm^{-1}K^{-1}) 6 mm thick, which are put together under some pressure. The two large surfaces in contact are mirror-like polished. In order to calibrate the air gap between the plates, nickel tapes 25, 10, 5, 2.5 and 1 μm thick are placed between the carbon layers. They represent thermal resistances of 10^{-3}, 4×10^{-4}, 2×10^{-4}, 10^{-4} and 4×10^{-5} m^{2}K/W respectively. The main advantage of using glassy carbon is that this material is at the same time highly absorbing at visible wavelengths and highly emitting at IR wavelengths. This means that its surface does not need to be prepared (painted or coated) in order to obtain a high enough signal to noise ratio, as it happens with metals and alloys.

In Figs. 9a and 9b we show the amplitude and phase thermograms corresponding to a 1 μm thick crack obtained with the following experimental parameters: f = 0.6 Hz, d ≈ 0.65 mm and a ≈ 0.35 mm. It is remarkable that such a thin crack is clearly featured using lock-in thermography. In Figs. 9c and 9d we show by dots the temperature profiles along the y axis. The continuous lines are the least squares fits to Eq. (10) using three free parameters: P_o, a and R_{th}. The values of Ln|T| and Ψ of each profile have been shifted to better appreciate the jump at the crack. Note that the fit quality is better for Ln|T| than for Ψ. This is because the jump at the crack is much higher for Ln|T| than for Ψ. All measurements shown in Figs. 9c and 9d have been performed with f = 0.6 Hz, d ≈ 0.65 mm and a ≈ 0.35 mm. The retrieved thermal resistance values are 8.0×10^{-4}, 4.2×10^{-4}, 2.2×10^{-4}, 9.8×10^{-5} and 4.5×10^{-5} m^{2}K/W, which correspond to air thicknesses of 21, 11, 5.7, 2.6 and 1.2 μm respectively. They are very close to the nominal values of the nickel tape thicknesses. On the other hand, in all fittings the radius of the laser spot is in the range a = 0.35-0.37 mm. To assess the robustness of the procedure we have performed complementary measurements changing the modulation

frequency f = 4.4 Hz, the distance between the spot and the crack d = 1.2 mm and the laser focus a = 0.82 mm. In all cases we have obtained the same thermal resistance, within an experimental uncertainty of ±15%.

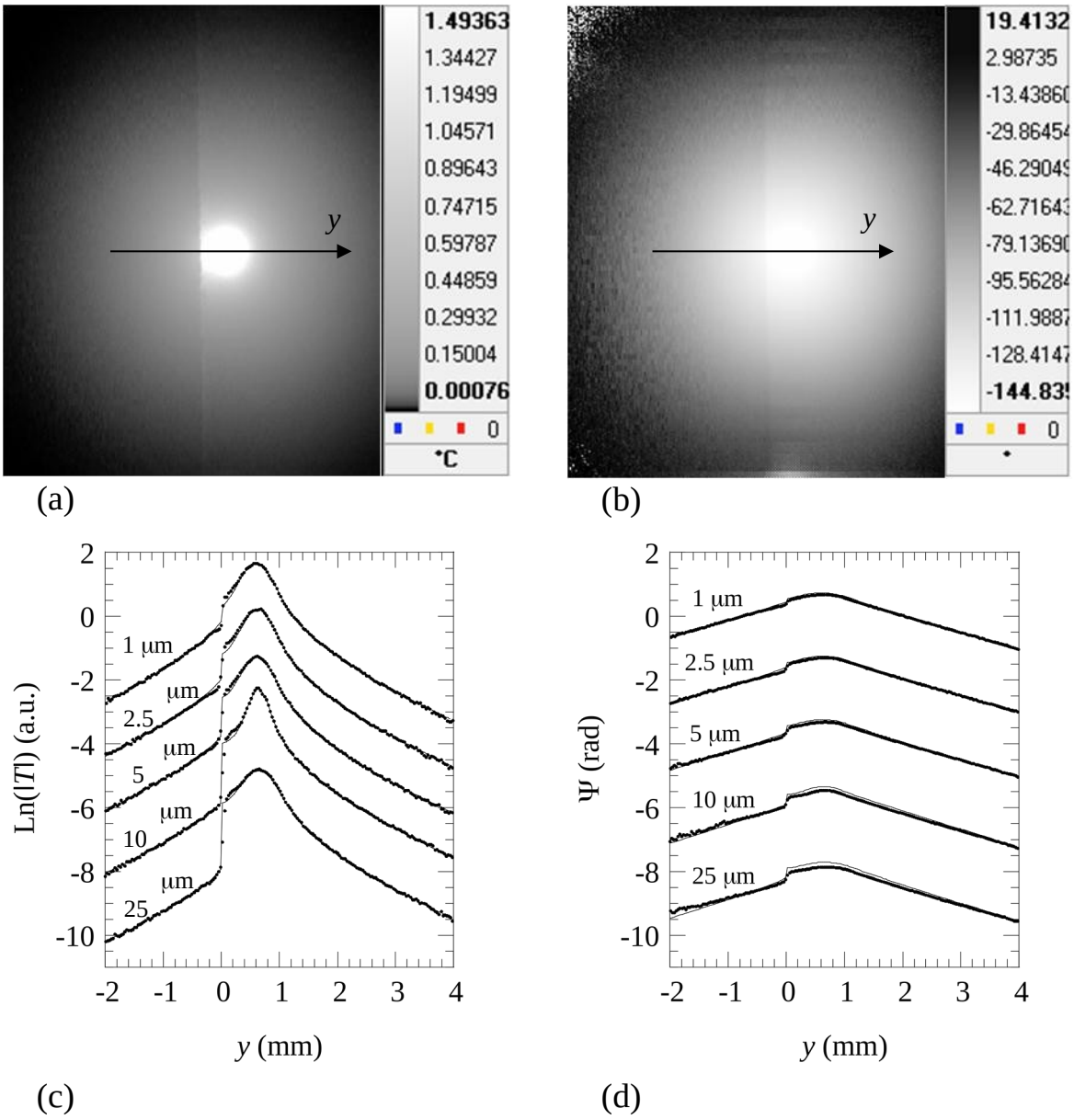

Figure 9. (a) Amplitude and (b) phase thermograms for two glassy carbon plates put in contact to simulate an infinite vertical crack 1 μm thick. The following experimental parameters have been used: d = 0.65 mm, a = 0.35 mm and f = 0.6 Hz. (c) Experimental natural logarithm of the surface temperature amplitude and (d) phase profiles along the y axis for several crack widths. Dots correspond to experimental data and continuous lines to the fit to Eq. (10).

We have performed the same kind of measurements in two blocks of AISI-304 2 cm thick. As this metallic alloy has a shiny surface, a thin graphite layer about 3 μm thick has been deposited onto the surface in order to increase both the absorption to the heating laser and the emissivity to infrared wavelengths. The amplitude and phase thermograms corresponding to a 1 μm thick crack are shown in Figs. 10 a and 10b. The same experimental parameters as in Fig. 9 have been used. The temperature profiles along the y-axis together

with the fits to Eq. (10) are shown in Figs. 10c and 10d. We have obtained the following thermal resistance values: 7.0×10^{-4}, 4.7×10^{-4}, 2.0×10^{-4}, 1.1×10^{-4}, 3.5×10^{-5} m^2K/W, which correspond to air gaps of 27, 12, 5.2, 2.8 and 0.9 μm respectively. As in the case of the glassy carbon, they are very close to the thicknesses of the nickel tapes.

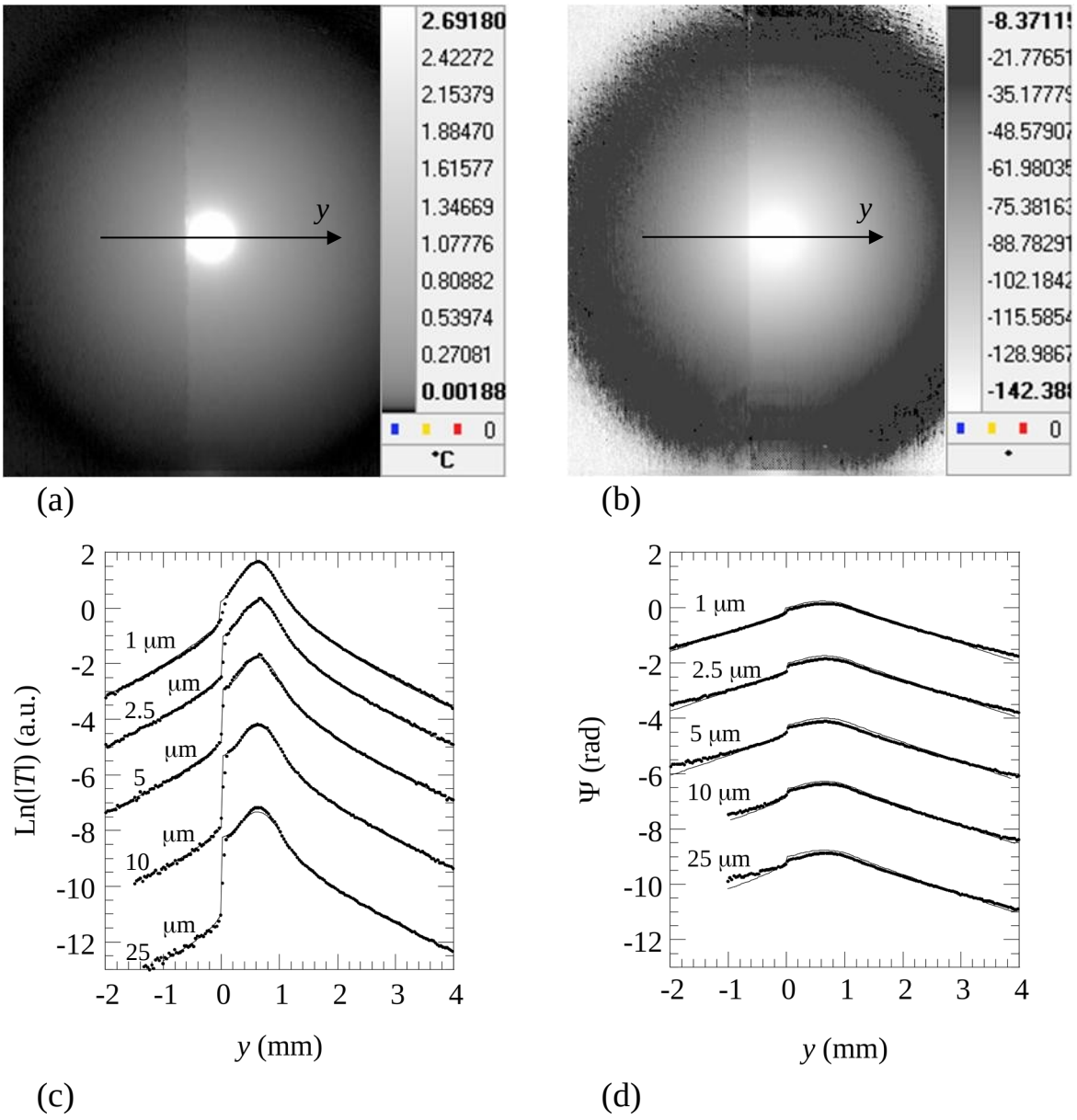

Figure 10. The same as in Fig. 9 for AISI-304 stainless steel.

Finally, we have put the two glassy carbon plates in direct contact, i.e. without inserting nickel plates. As the surfaces in contact are polished, they simulate an extremely thin crack. The result depends slightly on the position in which the sample is excited. At some positions we observe neither temperature amplitude contrast nor phase contrast. Moving the positions of the excitation spot on the same sample, we have obtained amplitude and phase contrasts corresponding to air gaps below 300 nm, probably due to different surface conditions. At the locations where we do not detect the crack, it remains undetectable even when the modulation is increased up to 100 Hz and the laser beam is focused down to 100

μm. This result allows us to conclude that the upper limit for this thermal resistance is $R_{th} \leq 10^{-6}$ m^{2}K/W.

It is worth noting that detecting very narrow cracks requires using a high frequency together with a laser beam tightly focused close to the crack. However, in our infrared thermography setup the spatial resolution is 30 μm so measurements with a thermal diffusion length $\mu < 100$ μm are not allowed. Under these experimental conditions, thermal resistances verifying $KR_{th} \leq 1$ μm will remain undetectable.

Note that the experimental results shown in Figs. 9 and 10 do not exhibit a sharp discontinuity at the crack but a smooth transition involving around 4 pixels. This result is due to the imperfect imaging system of the IR camera (diffraction, multiple reflections, flare…). The so-called Point Spread Function (PSF) of the optical system quantifies its effect, which depends on the lens quality. As in our system the effect is quite small, it has not been taken into account in the fittings. Anyway, it is worth noting that the microscope lens (with a resolution of 30 μm) produces a much smaller PSF than a 50 mm focal length lens with two extension tubes (providing a comparable resolution of 40 μm), with more than 10 pixels affected.

5. Conclusions

In this work, we have dealt with the width characterization of infinite vertical cracks using lock-in thermography with optical excitation. First, we have found an analytical expression for the surface temperature of a material containing such a crack when a modulated and focused laser beam impinges close to the crack. Both circular and line Gaussian spots are studied. The presence of the crack produces an abrupt jump in the amplitude and phase of the surface temperature at the crack position. Numerical simulations indicate that the highest amplitude temperature contrast is produced when a, d and μ satisfy the following condition: $d \approx \mu \approx 1.25a$. The validity of the model has been tested by performing lock-in thermography measurements on stainless steel and vitreous carbon samples containing cracks of calibrated width. By fitting the amplitude and phase of the surface temperature to the analytical model, the width of the crack is obtained. The agreement between the optically calibrated width and the retrieved one is very good even for widths as narrow as 1 μm. In Part II of this work, the characterization of vertical cracks of finite size will be addressed.

Acknowledgments

This work has been supported by the Ministerio de Ciencia e Innovación (MAT2011-23811 and MTM2010-16917), by Gobierno Vasco (IT619-13), by UPV/EHU (UFI 11/55), by Diputación General de Aragón, by CINVESTAV Unidad Mérida and by CONACYT beca mixta.

References

[1] Kubiak E J, 1968 *Appl. Opt.* **7** 1743-8
[2] Rantala J, Wu D and Busse G 1996 *Res. Nondest. Eval.* **7** 215-28
[3] Favro L D, Han X, Ouyang Z, Sun G, Sui H and Thomas R L 2000 *Rev. Sci. Instrum.* **71** 2418-21.
[4] Piau J-M, Bendada A, Maldague X and Legoux J-G 2008 *Nondestr. Testing Eval.* **23** 109-20.
[5] Renshaw J, Chen J C, Holland S D and Thompson R B 2011 *NDT&E Int.* **44** 736-9.
[6] Mendioroz A, Castelo A, Celorrio R and Salazar A 2013 *Meas. Sci. Technol.* **24** 065601
[7] Morbidini M, Cawley P, Barden T, Almond D and Duffour Ph 2006 *J. Appl. Phys.* **100** 104905
[8] Weekes B, Cawley P, Almond D and Li T 2010 *AIP Conf. Proc.* **1211** 490-7.
[9] Wang Y Q, Kuo P K, Favro L D and Thomas R L 1990 *Springer Series in Optical Science, Photoacoustic and Photothermal Phenomena II* **62** 24-6.
[10] Bodnar JL, Egée M, Menu C, Besnard R, Le Blanc A, Pigeon M and Sellier J Y 1994 *J. de Physique IV, Colloque C7* **4** C7-591-4.
[11] Gruss C, Lepoutre F and Balageas D 1996 *Prog. Nat. Sci. Suppl. vol.* **6**, 173-6.
[12] Krapez J-C 1999 *Int. J. Therm. Sci.* **38** 769-79.
[13] Li T, Almond D P and Rees D A S 2011 *Meas. Sci. Technol.* **22** 035701
[14] Schlichting J, Ziegler M, Dey A, Maierhofer Ch and Kreutzbruck M 2011 *QIRT Journal* **8** 119-23.
[15] Li T, Almond D P and Rees D A S 2011 *NDT&E Int.* **44** 216-25.
[16] Burrows S E, Dixon S, Pickering S G, Li T and Almond D P 2011 *NDT&E Int.* **44** 589-96.
[17] Schlichting J, Maierhofer Ch and Kreutzbruck M 2012 *NDT&E Int.* **45** 133-40.
[18] Streza M, Fedala Y, Roger J P, Tessier G and Boue C 2013 *Meas. Sci. Technol.* **24** 045602
[19] Johnson C 2009 *Numerical Solution of Partial Differential Equations by the Finite Element Method* (Dover).
[20] McDonald F A, Wetsel G C and Jamieson G E 1986 *Can. J. Phys.* **64** 1265-8.
[21] Ocariz A, Sanchez-Lavega A, Salazar A, Fournier D and Boccara A C 1996 *J. Appl. Phys.* **80** 2968-82.
[22] Carslaw H S and Jaeger J C 1959 *Conduction of Heat in Solids* (Oxford: Oxford University Press) p. 20
[23] NIST Digital Library of Mathematical Functions. http://dlmf.nist.gov/, Release 1.0.8 of 2014-04-25.
[24] Breitenstein O and Langenkamp M 2003 *Lock-in Thermography* (Berlin: Springer) p. 32

Figure captions

Figure 1. Scheme of the infinite vertical crack (in gray) inside a semi-infinite sample. (a) Circular illumination and (b) line illumination.

Figure 2. Simulation of (a) the natural logarithm of the temperature amplitude and (b) phase along the *y* axis for a semi-infinite AISI-304 sample (D = 4 mm^2/s and K = 15 Wm^{-1}K^{-1}) containing an infinite vertical crack. The sample is illuminated at d = 1 mm with a circular Gaussian laser with a = 0.75 mm modulated at f = 1 Hz. The effect of the value of the thermal resistance R_{th} (m^{2}K/W) is shown.

Figure 3. The same as in Fig. 2, but for a line Gaussian laser.

Figure 4. Numerical simulation of the dependence of Δ on the thermal contact resistance R_{th}. Calculations are performed for an AISI-304 material (D = 4 mm^2/s and K = 15 Wm^{-1}K^{-1}) with $d = \mu$ and $a = \mu/2$. Three modulation frequencies are tested. Continuous lines correspond to $\Delta_{|T|}$ and dashed lines to Δ_{Ψ}.

Figure 5. The same as in Fig. 4 with a fixed frequency f = 1 Hz. Continuous lines correspond to $\Delta_{|T|}$ and dashed lines to Δ_{Ψ}. Three combinations of laser distance and radius are analyzed: (1) $d = \mu$ and $a = \mu/2$, (2) $d = \mu$ and $a = \mu$, and (3) $d = \mu/2$ and $a = \mu/4$.

Figure 6. Numerical simulation of the dependence of Δ on the laser radius a. Calculations are performed for an AISI-304 sample with $d = \mu$. Three R_{th} values are analyzed: 10^{-5}, 10^{-4} and 10^{-3} m^{2}K/W. The continuous line corresponds to $\Delta_{|T|}$ and the dashed line to Δ_{Ψ}.

Figure 7. Numerical simulation of the dependence of Δ on the distance of the laser spot to the crack. Calculations have been performed for an AISI-304 sample (D = 4 mm^2/s and K = 15 Wm^{-1}K^{-1}) with $a = 0.75\mu$ and f = 1 Hz. Three R_{th} values are analyzed: 10^{-5}, 10^{-4} and 10^{-3} m^{2}K/W. The continuous line corresponds to $\Delta_{|T|}$ and the dashed line to Δ_{Ψ}.

Figure 8. Diagram of the experimental setup. AOM is the acousto-optic modulator and M is the microscope objective.

Figure 9. (a) Amplitude and (b) phase thermograms for two glassy carbon plates put in contact to simulate an infinite vertical crack 1 μm thick. The following experimental parameters have been used: d = 0.65 mm, a = 0.35 mm and f = 0.6 Hz. (c) Experimental natural logarithm of the surface temperature amplitude and (d) phase profiles along the *y* axis for several crack widths. Dots correspond to experimental data and continuous lines to the fit to Eq. (10).

Figure 10. The same as in Fig. 9 for AISI-304 stainless steel.